



# Integrating Pt@Ni(OH)<sub>2</sub> nanowire and Pt nanoparticle on C<sub>3</sub>N<sub>4</sub> with fast surface kinetics and charge transfer towards highly efficient photocatalytic water splitting

Shangcong Sun<sup>a,b</sup>, Yibin Feng<sup>a</sup>, Lun Pan<sup>a,b,\*</sup>, Xiangwen Zhang<sup>a,b</sup>, Ji-Jun Zou<sup>a,b,\*</sup>

<sup>a</sup> Key Laboratory for Green Chemical Technology of the Ministry of Education, School of Chemical Engineering and Technology, Tianjin University, Tianjin 300072, China

<sup>b</sup> Collaborative Innovative Center of Chemical Science and Engineering (Tianjin), Tianjin 300072, China

## ARTICLE INFO

### Keywords:

Photocatalysis  
Water splitting  
Cocatalyst  
Nickel hydroxide  
Carbon nitride

## ABSTRACT

Overall water splitting is vital in solar-hydrogen conversion. In addition to charge separation, the regulation of surface kinetics and suppression of backward reaction become particularly crucial. Herein, an all-in-one Pt@Ni(OH)<sub>2</sub>/C<sub>3</sub>N<sub>4</sub> photocatalyst is proposed by integrating Pt@Ni(OH)<sub>2</sub> composited nanowires and isolated Pt clusters on C<sub>3</sub>N<sub>4</sub>. In this heterostructure, Pt@Ni(OH)<sub>2</sub> with rich coordinatively unsaturated sites effectively boost O<sub>2</sub> evolution, and Pt-O-Ni interaction retards O–O bond cleavage thus inhibiting backward H<sub>2</sub>O regeneration. Meanwhile isolated Pt forms an Schottky junction with C<sub>3</sub>N<sub>4</sub> for electron transfer and proton reduction. Consequently, Pt@Ni(OH)<sub>2</sub>/C<sub>3</sub>N<sub>4</sub> achieves stoichiometric water splitting with H<sub>2</sub>/O<sub>2</sub> evolution of 1330/632 μmol g<sup>−1</sup> h<sup>−1</sup>, and an outperforming AQE of 4.2% at 420 nm. Our work manifests that accelerating charge migration, inhibiting backward reaction and tuning surface kinetics are dominant in water splitting, for which a rational design of robust redox pathways is necessary.

## 1. Introduction

In view of increasing global energy demands and anthropogenic climate change, the pursuit of renewable and eco-friendly energy sources has become extremely important. Accordingly, water splitting is one of the most promising approaches to harvest solar light [1–3]. To this end, the development of efficient and stable photocatalytic systems to accomplish pure water splitting without sacrificial chemicals is one of the ultimate goals in sustainable energy research [4–6]. Among the materials employed for overall water splitting, one-step photoexcitation system, although very rare, is the simplest practical model with highest utilization of photons [1,7]. In principle, such kind of photocatalysts requires not only a thermodynamic prerequisite for semiconductors to have band positions straddling the H<sup>+</sup>/H<sub>2</sub> and O<sub>2</sub>/H<sub>2</sub>O, but also a kinetic demand for effective photogenerated charges to drive the redox reactions [4,8,9]. Also, the semiconductor should absorb more visible light to maximize the utilization of solar energy [10]. Owing to these restrictions, only a small portion of semiconductors can be valid for overall water splitting, including several rare metal-based materials such as TaON, SrTiO<sub>3</sub> and GaN:ZnO, whose optical and electronic properties are only tunable in a limited range [11–13]. The design and

fabrication of low-cost photocatalysts with more easily processable electronic and structural properties are still big challenges. Recently, carbon nitride (C<sub>3</sub>N<sub>4</sub>) is reported for both H<sub>2</sub> and O<sub>2</sub> half-water splitting reactions (HER and OER) due to its suitable band structure and relative narrow band gap of about 2.7 eV [14–18]. Nonetheless, integrating the two halves into a single functional C<sub>3</sub>N<sub>4</sub> capable of pure water splitting remains very rare, and often affording quite low efficiencies [19–21].

Charge transfer and surface reaction are both elemental steps in photocatalytic water splitting. Although extensive efforts have been devoted to boost charge migration, the regulation of surface kinetics is often overlooked in time of designing particular photocatalysts. Essentially, the latter depends on adsorption and dissociation of H<sub>2</sub>O molecules [22,23]. In previous work it has been demonstrated that a composited Pt-Ni(OH)<sub>2</sub> cocatalyst is capable of boosting H<sub>2</sub>O activation, which achieves an AQE of 1.8% at 420 nm. However, such single redox site will lead to inevitable carrier recombination and backward reaction, retarding the photocatalytic efficiency. Actually, the inhibition of H<sub>2</sub>/O<sub>2</sub> backward recombination is one of the dominant factors during water splitting, since both reductive H<sub>2</sub> and oxidative O<sub>2</sub> are produced at adjacent nanoscale sites (different from the two-electrode (photo)electrocatalytic systems) and conventional cocatalysts like

\* Corresponding authors at: Key Laboratory for Green Chemical Technology of the Ministry of Education, School of Chemical Engineering and Technology, Tianjin University, Tianjin 300072, China.

E-mail addresses: [panlun76@tju.edu.cn](mailto:panlun76@tju.edu.cn) (L. Pan), [jj\\_zou@tju.edu.cn](mailto:jj_zou@tju.edu.cn) (J.-J. Zou).

<https://doi.org/10.1016/j.apcatb.2019.118028>

Received 25 June 2019; Received in revised form 24 July 2019; Accepted 27 July 2019

Available online 01 August 2019

0926-3373/ © 2019 Elsevier B.V. All rights reserved.

metal Pt also catalyze the backward regeneration of  $\text{H}_2\text{O}$  [24–26]. Therefore, a rational integration of robust redox pathways toward cumulatively accelerating charge transfer, tuning surface kinetics and inhibiting reverse reaction is the key to achieve one-step overall water splitting.

In this work, we design an all-in-one  $\text{C}_3\text{N}_4$ -based photocatalyst to enhance  $\text{H}_2\text{O}$  activation and suppress backward reaction, through integrating Pt decorated  $\text{Ni}(\text{OH})_2$  nanowires ( $\text{Pt@Ni}(\text{OH})_2$ ) and isolated Pt nanoparticles over  $\text{C}_3\text{N}_4$ . The  $\text{Pt@Ni}(\text{OH})_2$  composite is capable of adsorbing  $\text{H}_2\text{O}$  and cleaving O–H bonds, and the electron transfer through Pt–O–Ni bond results in a higher oxidation state of Pt, which inhibits  $\text{H}_2$  back oxidation [25,26]. Also, the ultrafine nanowires with rich coordinatively unsaturated sites provide abundant active centers to boost  $\text{O}_2$  evolution kinetics [27,28]. Meanwhile isolated Pt nanoparticles form a Schottky junction with  $\text{C}_3\text{N}_4$  to accelerate  $\text{H}_2$  generation. Consequently, the precisely tailored dual redox pathways lead to a remarkable water splitting performance with an apparent quantum efficiency (AQE) of 4.2% at 420 nm, superior to most visible-response photoexcitation systems to date. Also, we corroborate that the acceleration of surface redox kinetics and suppression of backward reaction are predominant in photocatalytic water splitting, in addition to the well-known charge separation. Our work also implies that an enhanced coupling of charge separation and surface reaction is promising to improve the solar conversion efficiency.

## 2. Experimental section

### 2.1. Synthesis of photocatalysts

$\text{C}_3\text{N}_4$  was synthesized by thermal condensation of melamine (3 g) at  $550^\circ\text{C}$  for 4 h in air.  $\text{Ni}(\text{OH})_2/\text{C}_3\text{N}_4$  was fabricated by a hydrothermal method. Typically,  $\text{C}_3\text{N}_4$  (250 mg) was dispersed in water (50 mL), then a defined amount of  $\text{Ni}(\text{NO}_3)_2 \cdot 6\text{H}_2\text{O}$  and urea was added (weight ratio = 4:1). The mixture was ultrasonicated for 1 h, transferred to a 100 mL autoclave and heated at  $100^\circ\text{C}$  for 12 h. The obtained product was naturally cooled and washed with ethanol and water, and dried at  $40^\circ\text{C}$  under vacuum overnight. After that,  $\text{Pt@Ni}(\text{OH})_2/\text{C}_3\text{N}_4$  and  $\text{Pt-Ni}(\text{OH})_2/\text{C}_3\text{N}_4$  were prepared by *in-situ* selective photo-reduction of  $\text{PtCl}_6^{2-}$ . Typically,  $\text{Ni}(\text{OH})_2/\text{C}_3\text{N}_4$  (50 mg) was dispersed in aqueous solution (100 mL) containing  $\text{H}_2\text{PtCl}_6$ , the system was purged with Argon for 30 min and then irradiated for 2 h under 300 W Xe-lamp. The obtained photocatalyst was washed with ethanol and water, and dried at  $40^\circ\text{C}$  under vacuum overnight.

$\text{Pt}/\text{C}_3\text{N}_4$  was synthesized by a procedure similar to that of  $\text{Pt-Ni}(\text{OH})_2/\text{C}_3\text{N}_4$  while  $\text{C}_3\text{N}_4$  was used instead of  $\text{Ni}(\text{OH})_2/\text{C}_3\text{N}_4$ . And  $\text{Pt-Ni}(\text{OH})_2/\text{C}_3\text{N}_4$  was prepared similar to that of  $\text{Ni}(\text{OH})_2/\text{C}_3\text{N}_4$  but  $\text{Pt}/\text{C}_3\text{N}_4$  was used instead of  $\text{C}_3\text{N}_4$ .

### 2.2. Characterizations

X-ray diffraction (XRD) patterns were obtained by using Bruker AXS D8 advanced diffractometer equipped with  $\text{Cu K}\alpha$  radiation at a scanning rate of  $5^\circ \text{ min}^{-1}$ . Fourier transform infrared (FTIR) spectra were obtained on a Bruker Vertex-70 Fourier transform infrared spectrometer. Raman spectra were obtained on a Renishaw inVia reflex Raman spectrometer with an excitation wavelength at 532 nm. UV–vis diffuse reflectance spectra (DRS) were obtained from a Hitachi F-4600 fluorescence spectrophotometer equipped with a 60 mm diameter integrating sphere using  $\text{BaSO}_4$  as reference. Transmission electron microscopy (TEM) and electron energy loss spectroscopy (EELS) analyses were measured by Tecnai G2 F20 transmission electron microscope equipped with an EELS detector. Inductively coupled plasma optical emission spectrometry (ICP-OES) measurements were carried out on a VISTA-MPX EL02115765 instrument. Zeta potential was measured by Malvern Nano ZS Zetasizer. X-ray photoelectron spectroscopy (XPS) analysis was conducted on a PHI-1600 X-ray photoelectron

spectroscopy equipped with Al  $\text{K}\alpha$  radiation, the binding energy was calibrated by the  $\text{C1 s}$  peak (284.8 eV) and the step-length was set as 0.05 eV. Ultraviolet photoelectron spectroscopy (UPS) was measured by Thermo Fisher Scientific ESCALAB 250Xi equipped with He I source ( $h\nu = 21.22 \text{ eV}$ ) and a total instrumental energy resolution of 100 meV. Photoluminescence spectra were measured by a Shimadzu UV-2600 spectrophotometer with an excitation light at 325 nm. Fluorescence decay spectra were measured by FLS980 spectrometer at 298 K.

(Photo)electrochemical measurements were conducted on a CHI 660B electrochemical system using a standard three-electrode cell with a working electrode, a Pt counter electrode, a  $\text{Ag}/\text{AgCl}$  reference electrode and  $\text{Na}_2\text{SO}_4$  (0.5 mol/L) electrolyte solution. The working electrode was prepared by dip-coating same amount of photocatalyst slurry on F-doped tin oxide glass ( $1.5 \times 1.5 \text{ cm}^2$ ). Electrochemical impedance measurements were carried out with a sinusoidal ac perturbation of 0.5 V applied over the frequency of  $0.1\text{--}10^5 \text{ Hz}$ .

### 2.3. Photocatalytic tests

**Photocatalytic test:** Photocatalytic water splitting was carried out in a sealed Pyrex vessel (280 mL) with a flat window and a silicone rubber septum. Typically, the catalyst (20 mg) was added into ultrapure water (100 mL, with a resistivity higher than  $18.2 \text{ M}\Omega \text{ cm}^{-1}$ ) and ultrasonicated for 10 min. The system was first degassed by bubbling Argon for 30 min and then sealed. The reaction was conducted under a 300 W Xe-lamp (15 A, PerfectLight company) and the temperature was maintained at  $0.5^\circ\text{C}$ .  $\text{H}_2$  and  $\text{O}_2$  half reaction tests were carried out in the same experimental setup with TEOA (10 vol%) and  $\text{AgNO}_3$  (0.01 mol/L) as sacrificial agents, respectively. Gas products were analyzed by Bruker 450-GC gas chromatography equipped with 5A molecular sieve column and thermal conductive detector, using Argon as carrier gas.  $\text{H}_2\text{O}_2$  was measured according to a reported *N,N*-diethyl-*p*-phenylenediamine oxidation method, which is based on the oxidation of *N,N*-diethyl-*p*-phenylenediamine (DPD) catalyzed with horseradish peroxidase (POD) by  $\text{H}_2\text{O}_2$  [29].

**Determination of AQE:** The measurement was performed by applying band-pass filters (FWHM = 15 nm) to control the wavelength of incident light. The reaction time was 2 h. Light intensity was measured by a UV–A radiometer (Photoelectric Instrument Factory, Beijing Normal University, model UV–A). The light intensities were 1.8, 2.8, 3.6, 4.7,  $4.5 \text{ mW cm}^{-2}$  at 365, 400, 420, 450, 500 nm, respectively. The AQE was calculated as follows:

where  $N_e$  is the number of reacted electrons,  $N_p$  is the number of incident photons.

**Photo-deposition of Au and  $\text{PbO}_2$ :** The photocatalyst (20 mg) was dispersed in aqueous solution (100 mL) containing  $\text{HAuCl}_4$  (0.18 mg) or  $\text{Pb}(\text{NO}_3)_2$  (0.15 mg) under magnetic stirring. After irradiating under 300 W Xe-lamp for 1 h, the powder was separated, washed and dried for further characterization.

### 2.4. $\text{H}_2$ and $\text{O}_2$ backward recombination test

The experiment was conducted according to literatures [26,30]. The photocatalyst (20 mg) was dispersed with ultrapure water (100 mL) in the same Pyrex vessel, purged with Argon for 30 min and then sealed.  $\text{H}_2$  (2 mL) and  $\text{O}_2$  (1 mL) were injected with the time set as 0, kept stirring during the test. The amount of  $\text{H}_2$  and  $\text{O}_2$  remained in the gas were analyzed by gas chromatography.

## 3. Results and discussion

### 3.1. Fabrication and structure of $\text{Pt-Ni}(\text{OH})_2/\text{C}_3\text{N}_4$

The  $\text{Pt-Ni}(\text{OH})_2/\text{C}_3\text{N}_4$  is designed to simultaneously combine  $\text{Pt@Ni}(\text{OH})_2$  composited nanowires and isolated Pt nanoparticles at single semiconductor (Scheme 1).  $\text{C}_3\text{N}_4$  used here was prepared by thermal

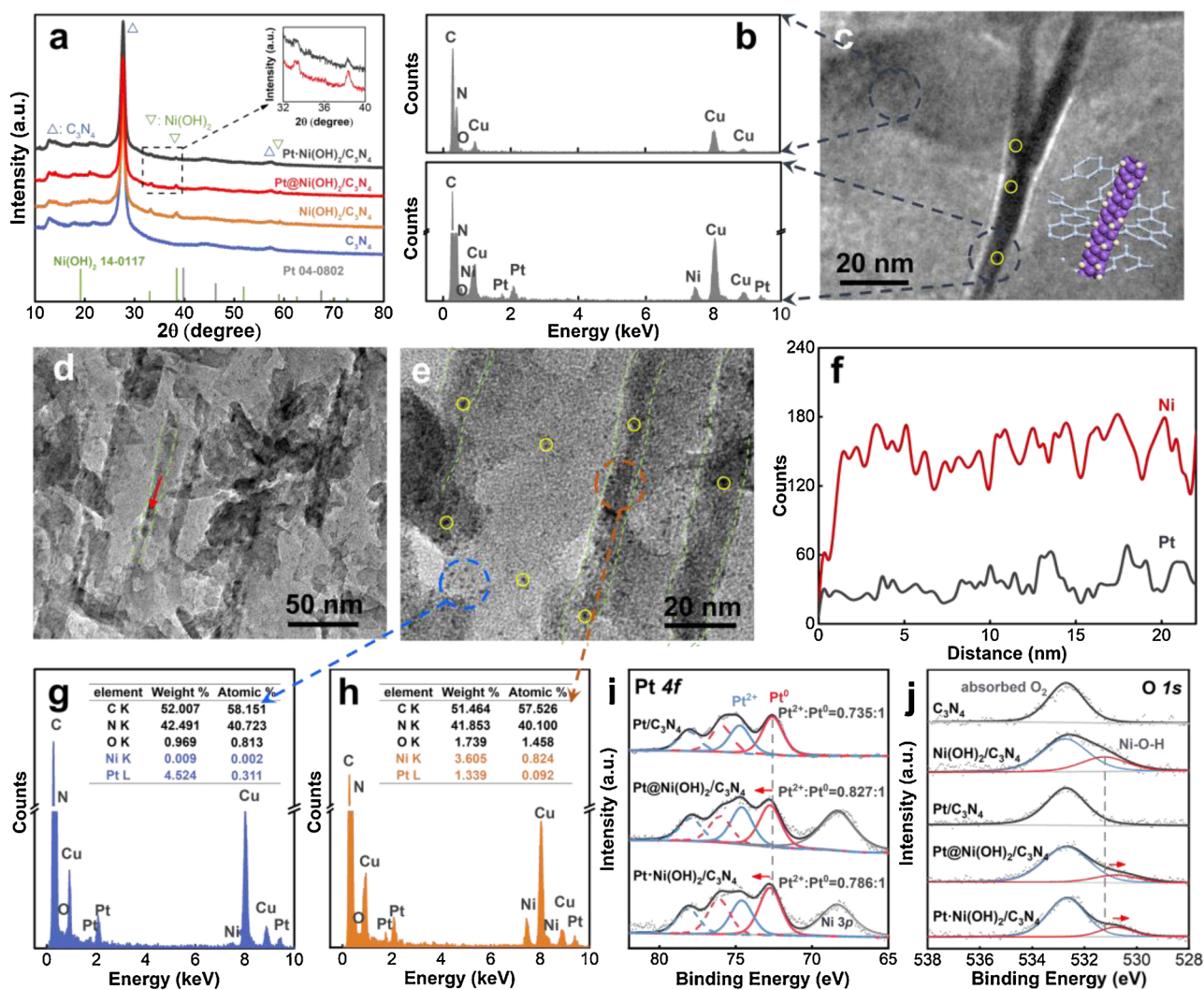
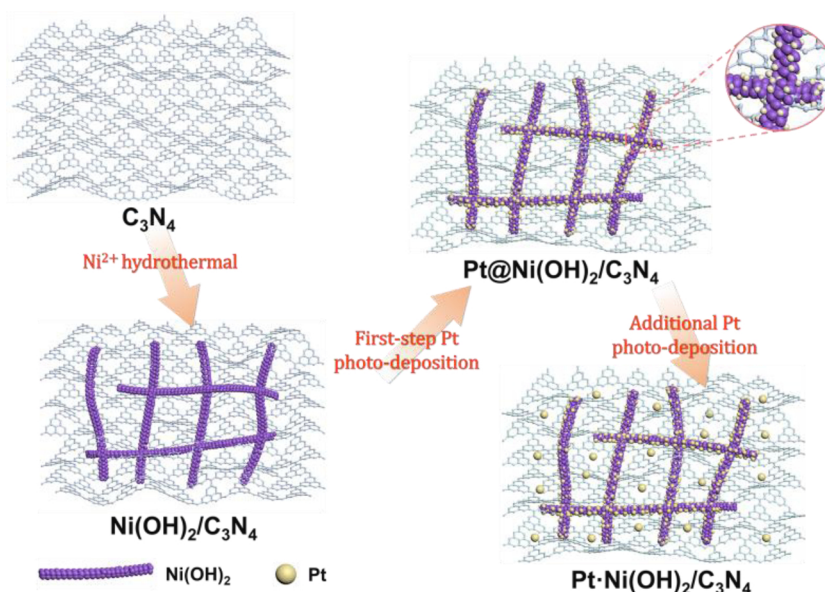


**Fig. 1.** (a) XRD patterns of the fabricated photocatalysts. (b) EDX point analyses and (c) TEM image of Pt@Ni(OH)<sub>2</sub>/C<sub>3</sub>N<sub>4</sub>. (d–e) TEM images and (f) EDX line-scan analysis (red line marked in d), (g–h) EDX point analyses of corresponding area marked (blue and orange circles) in e of Pt-Ni(OH)<sub>2</sub>/C<sub>3</sub>N<sub>4</sub>. (i) Pt 4f and (j) O 1s XPS spectra of the photocatalysts (For interpretation of the references to colour in this figure legend, the reader is referred to the web version of this article).



condensation of melamine. And corresponding XRD pattern in Fig. 1a shows typical characteristic peaks at  $13.2^\circ$  (100),  $27.6^\circ$  (002) (JCPDS 87–1526) [31]. This structure is also verified with FTIR and Raman spectroscopy (Fig. S1) [32]. UV–vis DRS spectrum of  $C_3N_4$  shows an optical absorption edge at 450 nm with band gap of 2.78 eV estimated from Kubelka-Munk function (Fig. S2), endowing it with well response to solar light. Then  $Ni(OH)_2$  nanowires were *in-situ* grown on  $C_3N_4$  ( $Ni(OH)_2/C_3N_4$ , the loading amount of  $Ni(OH)_2$  is 5.0 wt% based on  $C_3N_4$  if not specified) with nickel salt and urea as precursors via hydrothermal treatment. XRD pattern of this material is similar to pure  $C_3N_4$ , and the new peaks at  $33.1^\circ$  (100) and  $38.5^\circ$  (101) are well-matched with the standard card of  $\beta$ - $Ni(OH)_2$  (JCPDS 14-0117) [33]. Importantly, as seen from TEM images in Fig. 1,  $Ni(OH)_2$  possesses nanowire-like structure of about 5–15 nm in diameter and forms an intimate heterocomposite with  $C_3N_4$ . Such structure can lead to an increased charge transfer and provide more active sites as compared with the nanoparticle-like cocatalyst. In the next step, *in-situ* selective  $PtCl_6^{2-}$  photo-reduction was carried out to obtain  $Pt@Ni(OH)_2$  composite on  $C_3N_4$  (donated as  $Pt@Ni(OH)_2/C_3N_4$ , the amount of Pt is 0.3 wt% if not specified). No Pt signal is detected from XRD pattern mainly due to its low content. Moreover, TEM image and corresponding energy dispersive X-ray (EDX) spectra of  $Pt@Ni(OH)_2/C_3N_4$  show that Pt is exclusively deposited on  $Ni(OH)_2$ , and no Pt can be detected on bare  $C_3N_4$  plane (Fig. 1b and 1c). The formation of the composited nanowires mainly originates from electrostatic interaction, i.e.  $Ni(OH)_2$  is positively charged (with Zeta potential of 13.1 mV in water) while  $C_3N_4$  shows negative surface charge (with Zeta potential of -12.1 mV in water) from Zeta potential measurements. Therefore  $PtCl_6^{2-}$  anions are preferably adsorbed on  $Ni(OH)_2$  by electrostatic attraction and then *in-situ* reduced.

Following the decoration of  $Pt@Ni(OH)_2$ , isolated Pt nanoparticles were anchored on  $C_3N_4$  as reduction sites to get the final  $Pt-Ni(OH)_2/C_3N_4$ , which is realized by simply increasing the amount of  $PtCl_6^{2-}$  added in photo-deposition step (0.9 wt% Pt on  $C_3N_4$  in total if not specified). Since the adsorption capability of  $Ni(OH)_2$  to  $PtCl_6^{2-}$  anions is limited, the excessive non-adsorbed  $PtCl_6^{2-}$  will be reduced randomly on  $C_3N_4$  under irradiation. As shown in Fig. 1d and e, when 0.9 wt% Pt is added, part of Pt particles are orderly arranged along the nanowires while the others are directly dispersed on  $C_3N_4$  as isolated clusters. From Fig. 1f, the formation of  $Pt@Ni(OH)_2$  composite is identified by EDX elemental line-scan along the axial direction of nanowire (marked in Fig. 1d). This is also confirmed by EDX point analyses (Fig. 1g and h). Besides, the loading amount of Pt and  $Ni(OH)_2$  were further identified by ICP-OES measurement. For all the fabricated catalysts, the chemical structure and light absorption ability of  $C_3N_4$  appear unaltered as confirmed by FTIR and UV–vis DRS spectra (Fig. S3 and S4). The band structures obtained from UPS and Mott-Schottky measurements are also not changed as detailed in Fig. S5.

Above results confirm the successful construction of  $Pt-Ni(OH)_2/C_3N_4$  photocatalyst. Then XPS measurement was employed to get further insight into its chemical environment. Taking pristine  $C_3N_4$  as reference, the C 1s spectrum contains two peaks at 288.4 eV for C–N=C and at 284.8 eV for C–C bond, respectively (Fig. S6a). And the N 1s peak is deconvoluted into three peaks at 398.8 eV for N-pyridine moieties (C=N–C), at 399.9 eV for N–C<sub>3</sub> bonds and at 401.1 eV related to N–H moieties (Fig. S6b) [34].  $Ni^{2+}$  peaks are also observed for all  $Ni(OH)_2$ -containing samples (Fig. S6c), similar to the reported results [35]. Importantly, for  $Pt@Ni(OH)_2/C_3N_4$ , the ratio of  $Pt^{2+}/Pt^0$  is obviously higher than that of  $Pt/C_3N_4$  prepared by photo-deposition of 0.9 wt% Pt on  $C_3N_4$  (Fig. 1i). And the main Pt 4f peak of  $Pt@Ni(OH)_2/C_3N_4$  is slightly blue-shifted compared with  $Pt/C_3N_4$  [32]. In addition, in O 1s spectra (Fig. 1j), the binding energy of Ni–O–H in  $Pt@Ni(OH)_2/C_3N_4$  (530.8 eV) is 0.4 eV red-shifted compared with  $Ni(OH)_2/C_3N_4$  (531.2 eV). This is a sign of bonding effect in  $Pt@Ni(OH)_2$  nanowires where the electrons of Pt as donors interact with O atoms to form Pt–O–Ni bonds. The structure and electronic interaction are further

substantiated by EELS spectra (Fig. S7), which further demonstrate the strong interaction between Pt and  $Ni(OH)_2$  and that the chemical structure of  $C_3N_4$  is not affected by loading dual cocatalysts. The bonding states bring up strong synergetic effect to promote the adsorption of  $H_2O$  molecule and cleavage of O–H bonds in the initial step of water splitting, leading to an enhanced  $O_2$  formation kinetics [24,25,36]. And the more oxidized Pt state is capable of suppressing undesirable  $H_2$  and  $O_2$  backward recombination [26]. Importantly, when  $Pt@Ni(OH)_2$  nanowires and isolated Pt nanoparticles are integrated on  $C_3N_4$ ,  $Pt-Ni(OH)_2/C_3N_4$  possesses the characteristics of both  $Pt@Ni(OH)_2/C_3N_4$  and  $Pt/C_3N_4$ , which is expected to greatly boost the water splitting performance.

### 3.2. Charge transfer pathways and redox active sites

The separation and transfer of photogenerated charges were further characterized. As shown by steady-state and time-resolved fluorescence spectra in Fig. S8 and 2a, in comparison with  $Pt/C_3N_4$  and  $Pt@Ni(OH)_2/C_3N_4$ ,  $Pt-Ni(OH)_2/C_3N_4$  exhibits a longest averaged fluorescent lifetime (1.72 ns), implying that the dual redox sites are most efficient in accelerating charge transfer [37,38]. Moreover,  $Pt-Ni(OH)_2/C_3N_4$  exhibits a distinct decrease in the arc radius from electrochemical impedance spectra (Fig. 2b), and endows a highest current density from photocurrent response curves (Fig. 2c), indicating its remarkably reduced charge transfer resistance.

For in-depth determination of charge transfer pathways and redox active sites in photocatalysis, selective metal(oxide) photo-deposition test was conducted. We employed  $HAuCl_4$  and  $Pb(NO_3)_2$  as indicators for reduction and oxidation sites, respectively [14]. For  $Pt-Ni(OH)_2/C_3N_4$ ,  $PbO_2$  particles are preferably deposited on  $Pt@Ni(OH)_2$  nanowires while Au are only observed on  $C_3N_4$  surface near Pt domains, as revealed by Fig. 2d, 2e and S9. These results support the formation of dual redox pathways over  $C_3N_4$ . Basically,  $C_3N_4$  generates charges (holes and electrons) under illumination, then holes migrate to  $Pt@Ni(OH)_2$  composited nanowires and participate in water oxidation while electrons to isolated Pt domains for reduction reaction (Fig. 2f). Specifically, for  $Pt@Ni(OH)_2/C_3N_4$ , both Au and  $PbO_2$  particles are observed along the  $Pt@Ni(OH)_2$  nanowires (Fig. S10), indicating that  $Pt@Ni(OH)_2$  composite serves as both reduction and oxidation sites without isolated Pt on semiconductor, which will lead to inevitable charge recombination as well as undesirable backward recombination of the generated  $H_2$  and  $O_2$ .

The role of dual redox sites is further revealed by photocatalytic  $H_2$  and  $O_2$  evolution tests, which were conducted with triethanolamine (TEOA) and  $AgNO_3$  as sacrificial agents, respectively. As shown in Fig. 2g, 2h and S11, the photocatalytic HER activity of  $Pt/C_3N_4$  is hundreds-fold increased than pure  $C_3N_4$  while the OER part is almost unchanged, confirming that only electrons transfer to Pt efficiently, as well as subsequent proton reduction. When  $Pt@Ni(OH)_2$  composite is anchored on  $C_3N_4$  ( $Pt@Ni(OH)_2/C_3N_4$ ), the HER activity is also improved but less than  $Pt/C_3N_4$ , and the OER activity is significantly enhanced, demonstrating the composited nanowire as bifunctional cocatalyst although more robust in OER. Predominantly, attributed to the synergy of Pt and  $Ni(OH)_2$  in  $H_2O$  activation to promote reaction kinetics, the  $O_2$  evolution rate of  $Pt@Ni(OH)_2/C_3N_4$  is obviously enhanced compared to  $Ni(OH)_2/C_3N_4$  (note that bare Pt is inactive for  $O_2$  evolution). Moreover,  $Pt-Ni(OH)_2/C_3N_4$  exhibits the highest HER and OER activity. Overall the order of activity for HER is  $Pt-Ni(OH)_2/C_3N_4 > Pt/C_3N_4 > Pt@Ni(OH)_2/C_3N_4 > Ni(OH)_2/C_3N_4 > C_3N_4$ , while for OER is  $Pt-Ni(OH)_2/C_3N_4 > Pt@Ni(OH)_2/C_3N_4 > Ni(OH)_2/C_3N_4 > Pt/C_3N_4 \sim C_3N_4$ . It can be seen that the co-deposition of  $Pt@Ni(OH)_2$  composited nanowires and isolated Pt nanoparticles is most effective in enhancing the half-reaction performance, mainly attributed to the promoted charge transfer and surface redox kinetics.

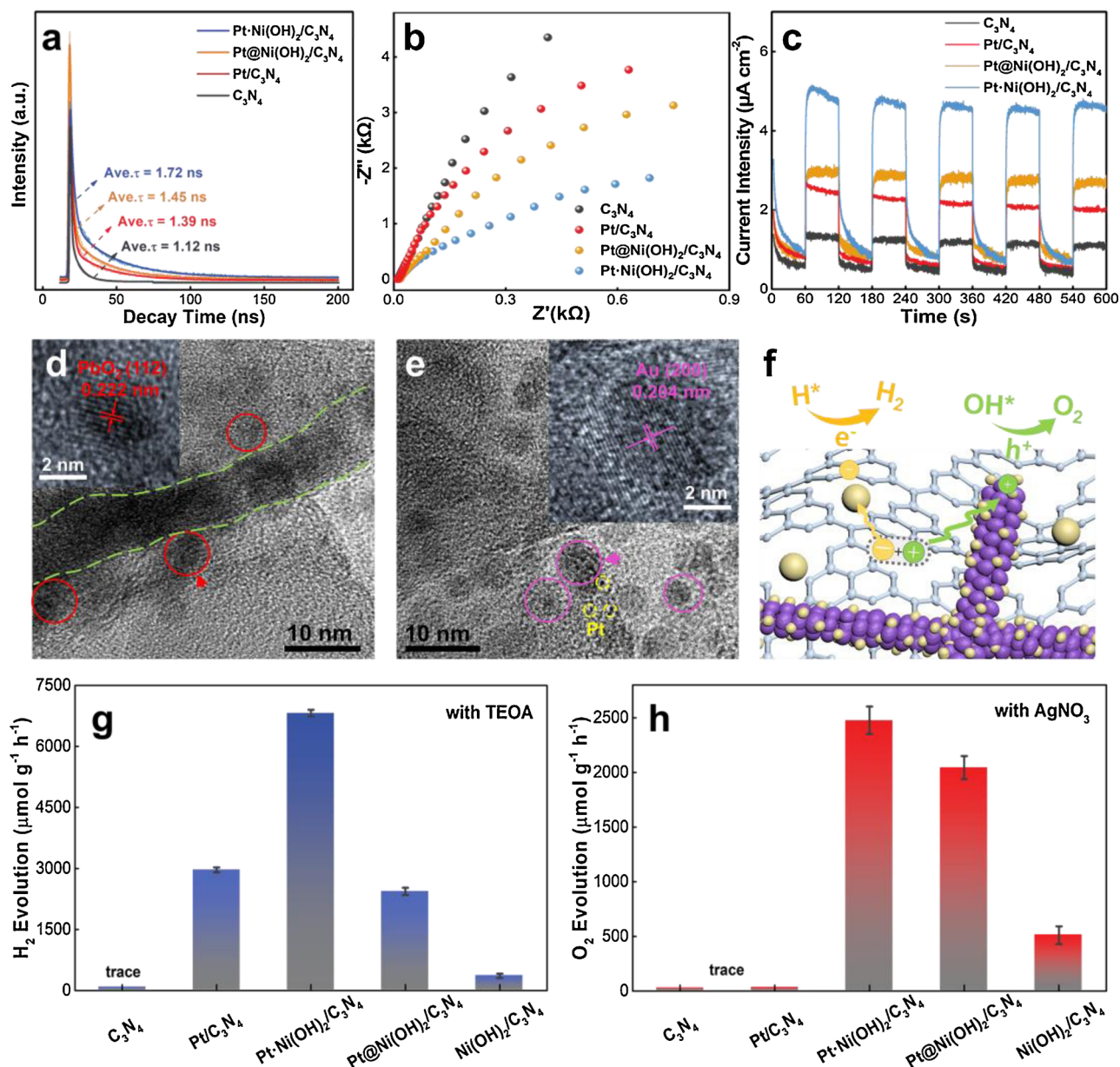


**Fig. 2.** (a) Time-resolved fluorescence spectra at 298 K, (b) electrochemical impedance spectroscopy Nyquist plots, (c) transient photocurrent response curves of fabricated photocatalysts. (d), (e) TEM images of Au and PbO<sub>2</sub> photo-deposited Pt-Ni(OH)<sub>2</sub>/C<sub>3</sub>N<sub>4</sub> in pure water. (f) Schematic diagram of charge transfer and redox reaction pathway. Photocatalytic (g) HER rate with TEOA and (h) OER rate with AgNO<sub>3</sub> of fabricated photocatalysts (average in 8 h for C<sub>3</sub>N<sub>4</sub> and Pt/C<sub>3</sub>N<sub>4</sub>, in 3 h for other samples).

### 3.3. Photocatalytic overall water splitting performance

The obtained samples were further tested for pure water splitting without any sacrificial or pH adjusting agents (Fig. 3a). As expected, pure C<sub>3</sub>N<sub>4</sub> cannot produce any H<sub>2</sub> or O<sub>2</sub> due to its fast charge recombination and deficiency in active sites. The incorporation of Pt on C<sub>3</sub>N<sub>4</sub> leads to an increase in HER activity but no OER activity. Pt@Ni(OH)<sub>2</sub>/C<sub>3</sub>N<sub>4</sub> shows an enhanced OER activity while only a little H<sub>2</sub> is generated. Especially, when Pt and Pt@Ni(OH)<sub>2</sub> are integrated onto C<sub>3</sub>N<sub>4</sub>, a stoichiometric production of H<sub>2</sub> and O<sub>2</sub> is achieved with HER rate of 1330  $\mu$ mol g<sup>-1</sup> h<sup>-1</sup> and OER rate of 632  $\mu$ mol g<sup>-1</sup> h<sup>-1</sup> (molar ratio of 2.1). Besides, the H<sub>2</sub> evolution rate reaches 604  $\mu$ mol g<sup>-1</sup> h<sup>-1</sup> under simulated sunlight (AM 1.5) and 298  $\mu$ mol g<sup>-1</sup> h<sup>-1</sup> under visible

light ( $\lambda > 400$  nm), realizing an efficient utilization of solar light (Fig. 3b). Also, as shown in Fig. 3c, Pt-Ni(OH)<sub>2</sub>/C<sub>3</sub>N<sub>4</sub> shows no obvious deactivation during stability test. XRD and XPS analyses of the recycled sample reveal no chemical change after reaction (Fig. S12 and S13), demonstrating its robust resistance to water and light corrosion. The apparent quantum efficiency closely follows the light absorption trend of the photocatalyst, revealing that the reaction is driven via photo-excitation (Fig. 3d). Importantly, Pt-Ni(OH)<sub>2</sub>/C<sub>3</sub>N<sub>4</sub> achieves an AQE of 4.2% at 420 nm, which is superior to most C<sub>3</sub>N<sub>4</sub> and other solid-state based photocatalysts to date (Table S2).

A sustainable water splitting requires simultaneous formation of H<sub>2</sub> and O<sub>2</sub> in stoichiometric ratio (2:1), thus necessitating a precise regulation between the reduction and oxidation sites. Here, the number of

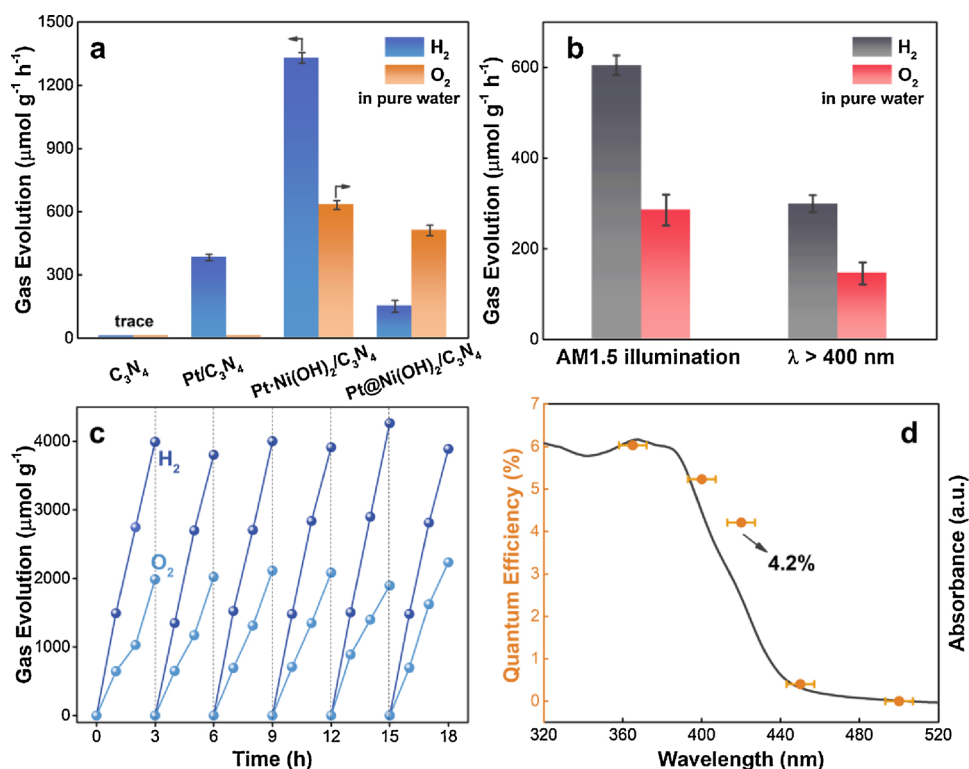


Fig. 3. (a) Averaged photocatalytic pure water splitting activities of different photocatalysts in 3 h. (b) Photocatalytic water splitting rates under simulated sunlight (AM 1.5) and visible light irradiation, (c) stability test and (d) wavelength-dependent AQE (orange dots) of Pt-Ni(OH)<sub>2</sub>/C<sub>3</sub>N<sub>4</sub>.

oxidation sites on Pt-Ni(OH)<sub>2</sub>/C<sub>3</sub>N<sub>4</sub> is tuned by adjusting the amount of Ni<sup>2+</sup> precursor added during the hydrothermal process, as more Ni(OH)<sub>2</sub> grown on C<sub>3</sub>N<sub>4</sub> will lead to more available Pt@Ni(OH)<sub>2</sub> nanowires. And the number of reduction sites is determined by the residual PtCl<sub>6</sub><sup>2-</sup> ions. As presented in Fig. 4a, with fixed amount of Pt, the number of oxidation sites increases with the amount of Ni(OH)<sub>2</sub> and the reduction sites are thereby decreased. Consequently, the H<sub>2</sub> and O<sub>2</sub> generation rates are obviously affected, both with volcano-type trend. In detail, although cocatalysts can accelerate charge migration and act as redox active sites, excessive cocatalysts may hinder the light absorption and charge generation of semiconductor, and act as charge recombination and H<sub>2</sub>/O<sub>2</sub> recombination centers, leading to a decrease in activity [21]. A stoichiometric result is reached only when the two kinds of redox pathways reach a balance, and even in other case the photocatalyst may produce more H<sub>2</sub> or O<sub>2</sub> in the initial stage, its activity declines rapidly. At higher or lower loading amount of Pt, the averaged water splitting activities remain relatively low with unbalanced production of H<sub>2</sub> and O<sub>2</sub> (Fig. S14). In detail, as shown in Fig. 4b, with relatively excessive isolated Pt nanoparticles, the ratio of generated H<sub>2</sub>/O<sub>2</sub> is about 4.8 in the first half hour, but the H<sub>2</sub> evolution rate decreases to only 20% after 3 h. By using the colorimetric DPD/POD method [29], it is found that a portion of holes oxidize H<sub>2</sub>O to H<sub>2</sub>O<sub>2</sub>, which is poisonous to C<sub>3</sub>N<sub>4</sub> (Fig. 4c). Small number of other radicals such as ·O<sub>2</sub><sup>-</sup> and ·OH may also be generated but hardly detected due to their short lifetime. On the other hand, with relatively excessive oxidation sites, the ratio of H<sub>2</sub>/O<sub>2</sub> is 1.6 in the first half hour, but the gas evolution rate also decreases with time (Fig. 4d). XPS spectra in Fig. 4e and S15 show that the relative intensity of C-C peak is obviously increased after reaction. In this situation, C<sub>3</sub>N<sub>4</sub> acts as sacrificing agent to react with the rest of electrons, resulting in a self-reduction. Overall, a precise regulation of redox pathways is the key to realize sustainable water splitting.

### 3.4. Importance of accelerating surface kinetics and suppressing backward reaction

It is well-known that accelerating charge transfer can efficiently enhance water splitting performance. Nonetheless, as an essential heterogeneous catalytic reaction, the acceleration of surface redox kinetics and suppression of backward reactions are also decisive. To prove this, we prepared a reference catalyst with exclusive spatially separated Pt nanoparticles and Ni(OH)<sub>2</sub> nanowires on C<sub>3</sub>N<sub>4</sub> through a similar preparation method (named as Pt-Ni(OH)<sub>2</sub>/C<sub>3</sub>N<sub>4</sub>, Fig. S16 and S17), which possesses identical Pt and Ni(OH)<sub>2</sub> content, similar cocatalyst morphologies and exposed active areas with Pt-Ni(OH)<sub>2</sub>/C<sub>3</sub>N<sub>4</sub>. UV-vis DRS, steady-state and time-resolved fluorescence spectra show that Pt-Ni(OH)<sub>2</sub>/C<sub>3</sub>N<sub>4</sub> exhibits a similar light absorption ability but higher charge separation efficiency compared to Pt-Ni(OH)<sub>2</sub>/C<sub>3</sub>N<sub>4</sub> (Fig. 5a, 5b and S18). Nevertheless, for Pt-Ni(OH)<sub>2</sub>/C<sub>3</sub>N<sub>4</sub>, the HER, OER and pure water splitting performance are only about 69%, 43% and 27% of Pt-Ni(OH)<sub>2</sub>/C<sub>3</sub>N<sub>4</sub>, respectively (Fig. 5c and 5d). Furthermore, Pt-Ni(OH)<sub>2</sub>/C<sub>3</sub>N<sub>4</sub> cannot realize stoichiometric gas formation and exhibits a gradually decreased reaction kinetics (Fig. S19). Considering the three cumulative steps in photocatalytic water splitting: light absorption, charge transfer and surface reaction, the enhanced activity of Pt-Ni(OH)<sub>2</sub>/C<sub>3</sub>N<sub>4</sub> can be attributed to the strengthened surface redox kinetics, since pure Pt or Ni(OH)<sub>2</sub> cannot activate and cleave H<sub>2</sub>O molecule as efficiently as composited Pt@Ni(OH)<sub>2</sub> [25,36].

Pt-Ni(OH)<sub>2</sub>/C<sub>3</sub>N<sub>4</sub> also exhibits a significant suppression ability towards H<sub>2</sub>/O<sub>2</sub> backward recombination. As shown in Figs. 5e and S20, a distinct decrease of H<sub>2</sub> and O<sub>2</sub> amount was observed on Pt-Ni(OH)<sub>2</sub>/C<sub>3</sub>N<sub>4</sub> photocatalyst, revealing the reverse reaction as a big obstacle during water splitting. However, for Pt-Ni(OH)<sub>2</sub>/C<sub>3</sub>N<sub>4</sub>, the H<sub>2</sub> and O<sub>2</sub> recombination rate is reduced by 50% as compared with that of Pt-Ni(OH)<sub>2</sub>/C<sub>3</sub>N<sub>4</sub>. Such superior property can be attributed to a restrained

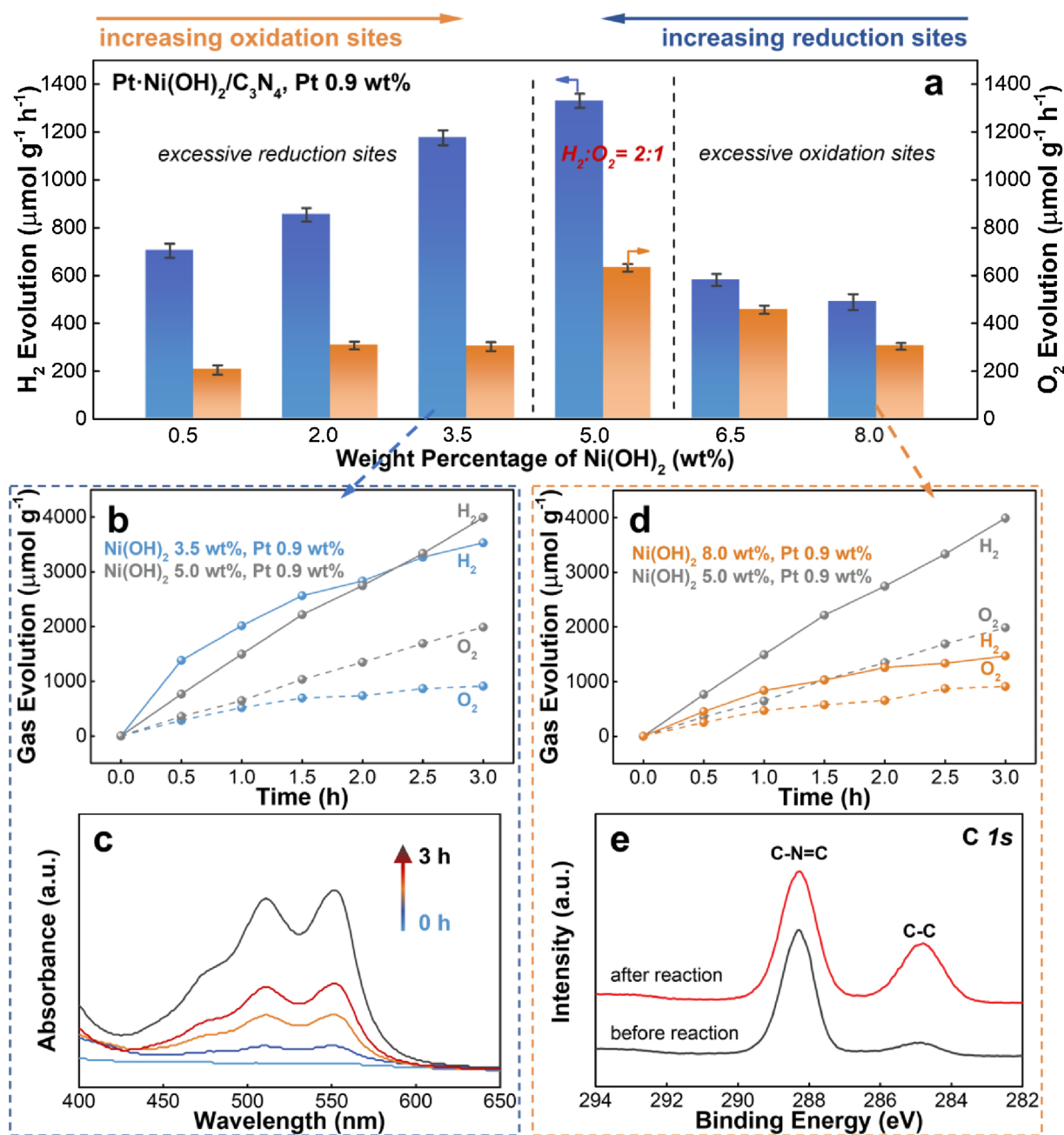


**Fig. 4.** (a) Photocatalytic pure water splitting rate of Pt-Ni(OH)<sub>2</sub>/C<sub>3</sub>N<sub>4</sub> (average in 3 h). (b) Time course of H<sub>2</sub>/O<sub>2</sub> evolution on Pt-Ni(OH)<sub>2</sub>/C<sub>3</sub>N<sub>4</sub> with relatively excess reduction sites (3.5 wt% Ni(OH)<sub>2</sub> and 0.9 wt% Pt) and (c) corresponding time-dependent UV-vis absorption spectra of the DPD/POD solution. (d) Time course of H<sub>2</sub>/O<sub>2</sub> evolution on Pt-Ni(OH)<sub>2</sub>/C<sub>3</sub>N<sub>4</sub> with relatively excess oxidation sites (8.0 wt% Ni(OH)<sub>2</sub> and 0.9 wt% Pt) and (e) corresponding C 1s XPS spectra of the photocatalyst before and after reaction.

adsorption and dissociation of O<sub>2</sub> and H<sub>2</sub> over the catalyst surface (specifically for the rate-determining step of O<sub>2</sub> dissociation) due to the presence of more oxidized Pt state in Pt-Ni(OH)<sub>2</sub>/C<sub>3</sub>N<sub>4</sub> [26].

#### 4. Conclusion

Photocatalytic water splitting relies on not only an efficient separation of photogenerated charges, but also simultaneous acceleration of surface redox kinetics and suppression of backward reactions. Herein, we present an all-in-one photocatalyst by integrating Pt@Ni(OH)<sub>2</sub> composited nanowires and isolated Pt nanoparticles on C<sub>3</sub>N<sub>4</sub>. On

the one hand, Pt@Ni(OH)<sub>2</sub> with rich coordinatively unsaturated sites possesses facile hole transfer pathways and abundant active centers. And the strong electronic interaction in Pt-O-Ni bond lowers the barrier for H<sub>2</sub>O activation to boost O<sub>2</sub> evolution kinetics. On the other hand, Pt/C<sub>3</sub>N<sub>4</sub> Schottky barrier effectively traps electrons and facilitates H<sub>2</sub> evolution. Moreover, the backward recombination of H<sub>2</sub> and O<sub>2</sub> is inhibited. Consequently, the constructed Pt-Ni(OH)<sub>2</sub>/C<sub>3</sub>N<sub>4</sub> exhibits a dramatic enhanced H<sub>2</sub> evolution rate of 1330 μmol g<sup>-1</sup> h<sup>-1</sup> and stoichiometric O<sub>2</sub> evolution of 632 μmol g<sup>-1</sup> h<sup>-1</sup> without any additional agents. The AQE reaches 4.2% at 420 nm, outperforming most reported visible-response photoexcitation systems. Our results imply the



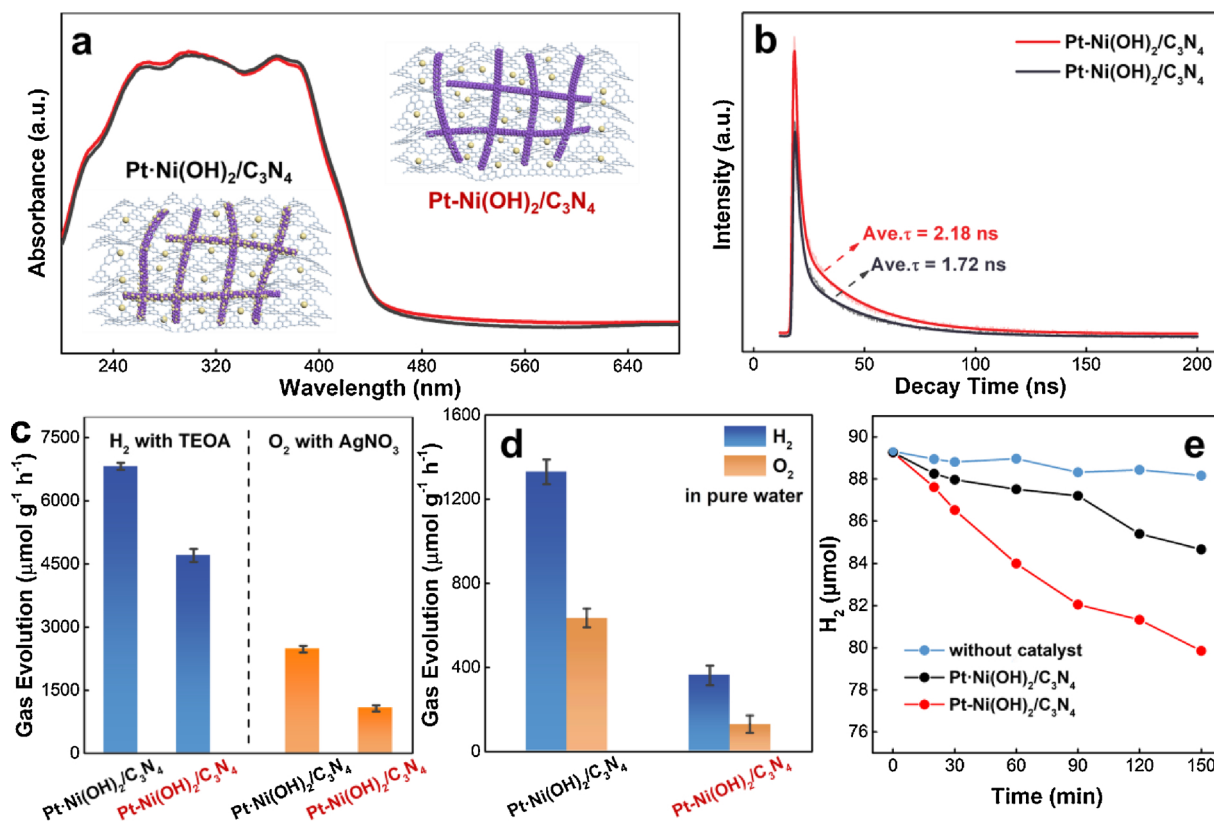


Fig. 5. (a) Structure diagrams and UV-vis DRS spectra, (b) time-resolved fluorescence kinetics at 298 K, (c) averaged photocatalytic HER rate with TEOA and OER rate with AgNO<sub>3</sub>, (d) averaged photocatalytic pure water splitting performance in 3 h and (e) H<sub>2</sub> and O<sub>2</sub> recombination test of Pt-Ni(OH)<sub>2</sub>/C<sub>3</sub>N<sub>4</sub> and Pt-Ni(OH)<sub>2</sub>/C<sub>3</sub>N<sub>4</sub>.

importance of modulating surface redox kinetics in photocatalytic water splitting, and provide new ideas into rational designing highly efficient photocatalysts.

#### Declaration of Competing Interest

The authors declare no conflict of interests.

#### Acknowledgements

The authors appreciate the support from the National Natural Science Foundation of China (21676193, 51661145026, 21506156).

#### Appendix A. Supplementary data

Supplementary material related to this article can be found, in the online version, at doi:<https://doi.org/10.1016/j.apcatb.2019.118028>.

#### References

- [1] Z. Wang, C. Li, K. Domen, Recent developments in heterogeneous photocatalysts for solar-driven overall water splitting, *Chem. Soc. Rev.* 48 (2019) 2109.
- [2] J. Qi, W. Zhang, R. Cao, Solar-to-hydrogen energy conversion based on water splitting, *Adv. Energy Mater.* 8 (2018) 1701620.
- [3] D. Kong, Y. Zheng, M. Kobielski, Y. Wang, Z. Bai, W. Macyk, X. Wang, J. Tang, Recent advances in visible light-driven water oxidation and reduction in suspension systems, *Mater. Today* 21 (2018) 897–924.
- [4] K. Maeda, Z-scheme water splitting using two different semiconductor photocatalysts, *ACS Catal.* 3 (2013) 1486–1503.
- [5] S.J.A. Moniz, S.A. Shevlin, D.J. Martin, Z.-X. Guo, J. Tang, Visible-light driven heterojunction photocatalysts for water splitting—a critical review, *Energy Environ. Sci.* 8 (2015) 731–759.
- [6] J. Low, C. Jiang, B. Cheng, S. Wageh, A.A. Al-Ghamdi, J. Yu, A review of direct Z-scheme photocatalysts, *Small Methods* 1 (2017) 1700080.
- [7] S. Chen, T. Takata, K. Domen, Particulate photocatalysts for overall water splitting, *Nat. Rev. Mater.* 2 (2017) 17050.
- [8] L. Wang, Y. Zhang, L. Chen, H. Xu, Y. Xiong, 2D polymers as emerging materials for

- photocatalytic overall water splitting, *Adv. Mater.* 30 (2018) 1801955.
- [9] S. Sun, G. Shen, J. Jiang, W. Mi, X. Liu, L. Pan, X. Zhang, J.-J. Zou, Boosting oxygen evolution kinetics by Mn-N-C motifs with tunable spin state for highly efficient solar-driven water splitting, *Adv. Energy Mater.* 9 (2019) 1901505.
- [10] C.-F. Fu, X. Wu, J. Yang, Material design for photocatalytic water splitting from a theoretical perspective, *Adv. Mater.* 30 (2018) 1802106.
- [11] W.-J. Chun, A. Ishikawa, H. Fujisawa, T. Takata, J.N. Kondo, M. Hara, M. Kawai, Y. Matsumoto, K. Domen, Conduction and valence band positions of Ta<sub>2</sub>O<sub>5</sub>, TaON, and Ta<sub>3</sub>N<sub>5</sub> by UPS and electrochemical methods, *J. Phys. Chem. B* 107 (2003) 1798–1803.
- [12] K. Maeda, T. Takata, M. Hara, N. Saito, Y. Inoue, H. Kobayashi, K. Domen, GaN:ZnO solid solution as a photocatalyst for visible-light-driven overall water splitting, *J. Am. Chem. Soc.* 127 (2005) 8286–8287.
- [13] T.K. Townsend, N.D. Browning, F.E. Osterloh, Overall photocatalytic water splitting with NiO<sub>x</sub>-SrTiO<sub>3</sub>—a revised mechanism, *Energy Environ. Sci.* 5 (2012) 9543–9550.
- [14] Z.-F. Huang, J. Song, X. Wang, L. Pan, K. Li, X. Zhang, L. Wang, J.-J. Zou, Switching charge transfer of C<sub>3</sub>N<sub>4</sub>/W<sub>18</sub>O<sub>49</sub> from Type-II to Z-Scheme by interfacial band bending for highly efficient photocatalytic hydrogen evolution, *Nano Energy* 40 (2017) 308–316.
- [15] Z.-F. Huang, J. Song, L. Pan, Z. Wang, X. Zhang, J.-J. Zou, W. Mi, X. Zhang, L. Wang, Carbon nitride with simultaneous porous network and O-doping for efficient solar-energy-driven hydrogen evolution, *Nano Energy* 12 (2015) 646–656.
- [16] G. Zhang, Q. Ji, Z. Wu, G. Wang, H. Liu, J. Qu, J. Li, Facile “spot-heating” synthesis of carbon dots/carbon nitride for solar hydrogen evolution synchronously with contaminant decomposition, *Adv. Funct. Mater.* 28 (2018) 1706462.
- [17] C. Ye, J.-X. Li, Z.-J. Li, X.-B. Li, X.-B. Fan, L.-P. Zhang, B. Chen, C.-H. Tung, L.-Z. Wu, Enhanced driving force and charge separation efficiency of protonated g-C<sub>3</sub>N<sub>4</sub> for photocatalytic O<sub>2</sub> evolution, *ACS Catal.* 5 (2015) 6973–6979.
- [18] G. Zhou, Y. Shan, Y. Hu, X. Xu, L. Long, J. Zhang, J. Dai, J. Guo, J. Shen, S. Li, L. Liu, X. Wu, Half-metallic carbon nitride nanosheets with micro grid mode resonance structure for efficient photocatalytic hydrogen evolution, *Nat. Commun.* 9 (2018) 3366.
- [19] G. Zhang, Z.-A. Lan, X. Wang, Surface engineering of graphitic carbon nitride polymers with cocatalysts for photocatalytic overall water splitting, *Chem. Sci.* 8 (2017) 5261–5274.
- [20] D. Zheng, X.-N. Cao, X. Wang, Precise formation of a hollow carbon nitride structure with a janus surface to promote water splitting by photoredox catalysis, *Angew. Chem. Int. Ed.* 55 (2016) 11512–11516.
- [21] J. Ran, J. Zhang, J. Yu, M. Jaroniec, S.Z. Qiao, Earth-abundant cocatalysts for semiconductor-based photocatalytic water splitting, *Chem. Soc. Rev.* 43 (2014) 7787–7812.
- [22] M. Tahir, L. Pan, F. Idrees, X. Zhang, L. Wang, J.-J. Zou, Z.L. Wang, Electrocatalytic oxygen evolution reaction for energy conversion and storage: a comprehensive



- review, *Nano Energy* 37 (2017) 136–157.
- [23] N. Mahmood, Y. Yao, J.-W. Zhang, L. Pan, X. Zhang, J.-J. Zou, Electrocatalysts for hydrogen evolution in alkaline electrolytes: mechanisms, challenges, and prospective solutions, *Adv. Sci.* 5 (2018) 1700464.
- [24] S. Sun, Y.-C. Zhang, G. Shen, Y. Wang, X. Liu, Z. Duan, L. Pan, X. Zhang, J.-J. Zou, Photoinduced composite of Pt decorated Ni(OH)<sub>2</sub> as strongly synergetic cocatalyst to boost H<sub>2</sub>O activation for photocatalytic overall water splitting, *Appl. Catal. B* 243 (2019) 253–261.
- [25] R. Subbaraman, D. Tripkovic, D. Strmcnik, K.-C. Chang, M. Uchimura, A.P. Paulikas, V. Stamenkovic, N.M. Markovic, Enhancing hydrogen evolution activity in water splitting by tailoring Li<sup>+</sup>-Ni(OH)<sub>2</sub>-Pt interfaces, *Science* 334 (2011) 1256–1260.
- [26] Y.H. Li, J. Xing, Z.J. Chen, Z. Li, F. Tian, L.R. Zheng, H.F. Wang, P. Hu, H.J. Zhao, H.G. Yang, Unidirectional suppression of hydrogen oxidation on oxidized platinum clusters, *Nat. Commun.* 4 (2013) 2500.
- [27] A.I. Hochbaum, P. Yang, Semiconductor nanowires for energy conversion, *Chem. Rev.* 110 (2010) 527–546.
- [28] J. Tian, N. Cheng, Q. Liu, W. Xing, X. Sun, Cobalt phosphide nanowires: efficient nanostructures for fluorescence sensing of biomolecules and photocatalytic evolution of dihydrogen from water under visible light, *Angew. Chem. Int. Ed.* 54 (2015) 5493–5497.
- [29] L. Shi, L. Yang, W. Zhou, Y. Liu, L. Yin, X. Hai, H. Song, J. Ye, Photoassisted construction of holey defective g-C<sub>3</sub>N<sub>4</sub> photocatalysts for efficient visible-light-driven H<sub>2</sub>O<sub>2</sub> production, *Small* 14 (2018) 1703142.
- [30] W. Meng, W. Zhen, B. Tian, J. Ma, G. Lu, The inhibition of hydrogen and oxygen recombination reaction by halogen atoms on over-all water splitting over Pt-TiO<sub>2</sub> photocatalyst, *Appl. Catal. B* 236 (2018) 240–252.
- [31] W.-D. Oh, L.-W. Lok, A. Veksha, A. Giannis, T.-T. Lim, Enhanced photocatalytic degradation of bisphenol A with Ag-decorated S-doped g-C<sub>3</sub>N<sub>4</sub> under solar irradiation: performance and mechanistic studies, *Chem. Eng. J.* 333 (2018) 739–749.
- [32] G. Zhang, Z.-A. Lan, L. Lin, S. Lin, X. Wang, Overall water splitting by Pt/g-C<sub>3</sub>N<sub>4</sub> photocatalysts without using sacrificial agents, *Chem. Sci.* 7 (2016) 3062–3066.
- [33] K. Zhu, H. Liu, M. Li, X. Li, J. Wang, X. Zhu, W. Yang, Atomic-scale topochemical preparation of crystalline Fe<sup>3+</sup>-doped β-Ni(OH)<sub>2</sub> for an ultrahigh-rate oxygen evolution reaction, *J. Mater. Chem. A* 5 (2017) 7753–7758.
- [34] L. Kong, Y. Ji, Z. Dang, J. Yan, P. Li, Y. Li, S.F. Liu, g-C<sub>3</sub>N<sub>4</sub> loading black phosphorus quantum dot for efficient and stable photocatalytic H<sub>2</sub> generation under visible light, *Adv. Funct. Mater.* 28 (2018) 1800668.
- [35] M. Gong, W. Zhou, M.-C. Tsai, J. Zhou, M. Guan, M.-C. Lin, B. Zhang, Y. Hu, D.-Y. Wang, J. Yang, S.J. Pennycook, B.-J. Hwang, H. Dai, Nanoscale nickel oxide/nickel heterostructures for active hydrogen evolution electrocatalysis, *Nat. Commun.* 5 (2014) 4695.
- [36] Y. Wang, H. Zhuo, X. Zhang, X. Dai, K. Yu, C. Luan, L. Yu, Y. Xiao, J. Li, M. Wang, F. Gao, Synergistic effect between undercoordinated platinum atoms and defective nickel hydroxide on enhanced hydrogen evolution reaction in alkaline solution, *Nano Energy* 48 (2018) 590–599.
- [37] S. Wang, B.Y. Guan, X. Wang, X.W.D. Lou, Formation of hierarchical Co<sub>9</sub>S<sub>8</sub>@ZnIn<sub>2</sub>S<sub>4</sub> heterostructured cages as an efficient photocatalyst for hydrogen evolution, *J. Am. Chem. Soc.* 140 (2018) 15145–15148.
- [38] Y. Yu, W. Yan, X. Wang, P. Li, W. Gao, H. Zou, S. Wu, K. Ding, Surface engineering for extremely enhanced charge separation and photocatalytic hydrogen evolution on g-C<sub>3</sub>N<sub>4</sub>, *Adv. Mater.* 30 (2018) 1705060.